

Chemistry of SO₂ and Organosulfur Molecules on Metal and Oxide Surfaces: Unraveling the Mysteries behind Catalyst Poisoning and Desulfurization

J.A. Rodriguez, J. Hrbek, T. Jirsak, J. Hanson and S. Chaturvedi (BNL)
 J.L. Brito (Venezuelan Institute of Scientific Research, IVIC)

Sulfur dioxide is one of the major air pollutants released to the atmosphere as a result of volcanic activity and the combustion of fuels in power plants, factories, houses and transportation. On the other hand, organosulfur molecules are common impurities in oil-derived feedstocks and poison many metal/oxide catalysts used in commercial processes. Millions of dollars are lost every year due to the negative effects of sulfur poisoning. In the Catalysis Group at the Chemistry Department of Brookhaven National Laboratory, experiments are being carried out to obtain a fundamental understanding of

the effects of sulfur on the structural, electronic and chemical properties of metal and oxide surfaces. This type of knowledge is necessary when designing catalysts that have a high efficiency for the destruction or removal of sulfur-containing molecules (DeSO_x and hydrodesulfurization processes), or when choosing catalysts that have a low sensitivity to sulfur poisoning. The research projects make extensive use of the unique facilities available at the NSLS for surface and materials characterization.

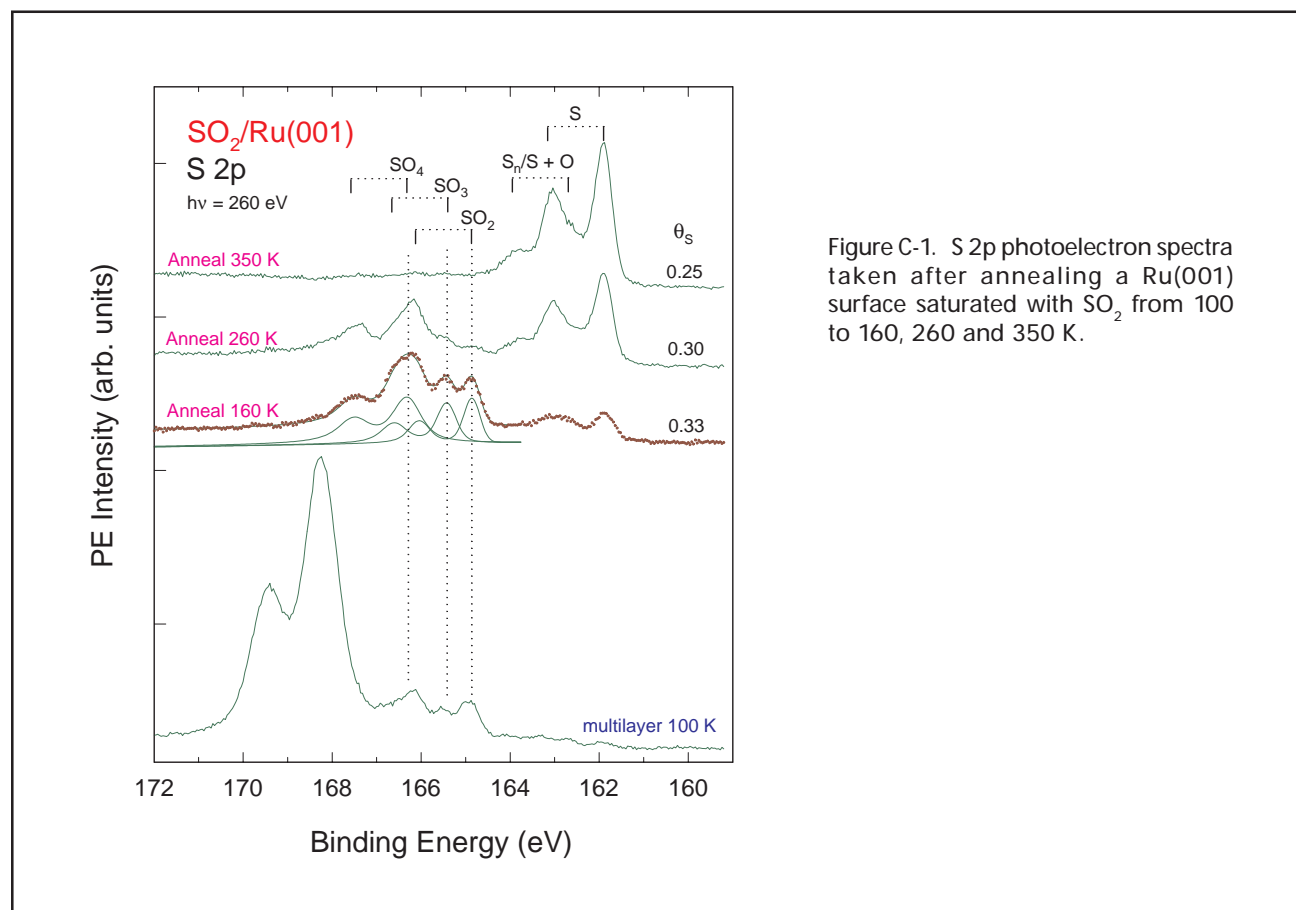


Figure C-1. S 2p photoelectron spectra taken after annealing a Ru(001) surface saturated with SO₂ from 100 to 160, 260 and 350 K.

The chemistry of sulfur dioxide on Pt(111),^[1] Rh(111),^[2] Ru(001),^[3] and Mo(110)^[4] was examined at temperatures between 100 and 500 K. In experiments performed at beamline U7A, several sulfur species with distinct electronic properties were identified (for example, see **Figure C-1**). On all the metals, SO₂ dissociates (SO_{2,a} → S_a + 2O_a) or transforms into SO₃ and SO₄ species. No evidence was found for the existence of S_O as a stable product. The reactivity of the metals increases following the sequence: Mo < Ru < Rh ≈ Pt. It was found that adsorption geometries in which SO₂ is di-coordinated via O,O or S,O are the most probable precursors for dissociation.

Metal-metal bonding can have a drastic impact on the chemical affinity of a metal for SO₂ and other sulfur-containing molecules.^[1,2,5,6] A Sn/Pt(111) alloy is much less reactive towards SO₂ (**Figure C-2**), H₂S, S₂, and thiophene than polycrystalline tin or clean Pt(111).^[1] The electronic perturbations that accompany the formation of Pt-Sn bonds reduce the electron-donor ability of Pt and Sn, and both metals are not able to respond in an effective way to the presence of molecules like SO₂ or H₂S.^[1,5] Among the common site blockers (Cu, Ag, Au, Al, Zn, Sn), tin is the best choice for reducing the sensitivity of Pt reforming catalysts to sulfur poisoning.^[1,5] In a similar way, Pd/Rh automotive exhaust catalysts can have a good catalytic activity and be more tolerant to the presence of sulfur-containing molecules in the gasoline than pure Pd catalysts.^[2] A Pd monolayer supported on Rh(111) is less chemically active than pure Pd or Rh(111) for the dissociation of SO₂ or thiophene.^[2] A very large drop in the reactivity of Pd can be expected when this metal is bonded to s,p or early-transition metals.^[2] All these results together indicate that bimetallic bonding can be a useful “tool” for increasing the sulfur tolerance of Pt and Pd based catalysts.^[1,2,5] On the other hand, in hydrodesulfurization processes metal-metal bonding can be useful for enhancing the activity of Mo-based catalysts in the removal or transformation of organosulfur molecules.^[6]

Since most poisoned catalyst are expensive, there is a need to reactivate them. Reaction with oxygen (S_{solid} + O_{2,gas} → SO_{2,gas}) is a promising route for regenerating pure oxide catalysts. The process is carried out under pressures of oxygen (0.2-2 atm) that are not compatible with most of the techniques currently used in surface science. One can study it using x-ray absorption near-edge spectroscopy (XANES) and x-ray diffraction (XRD).^[8,9] Investigations at beamline X7B have established the feasibility of conducting subminute,

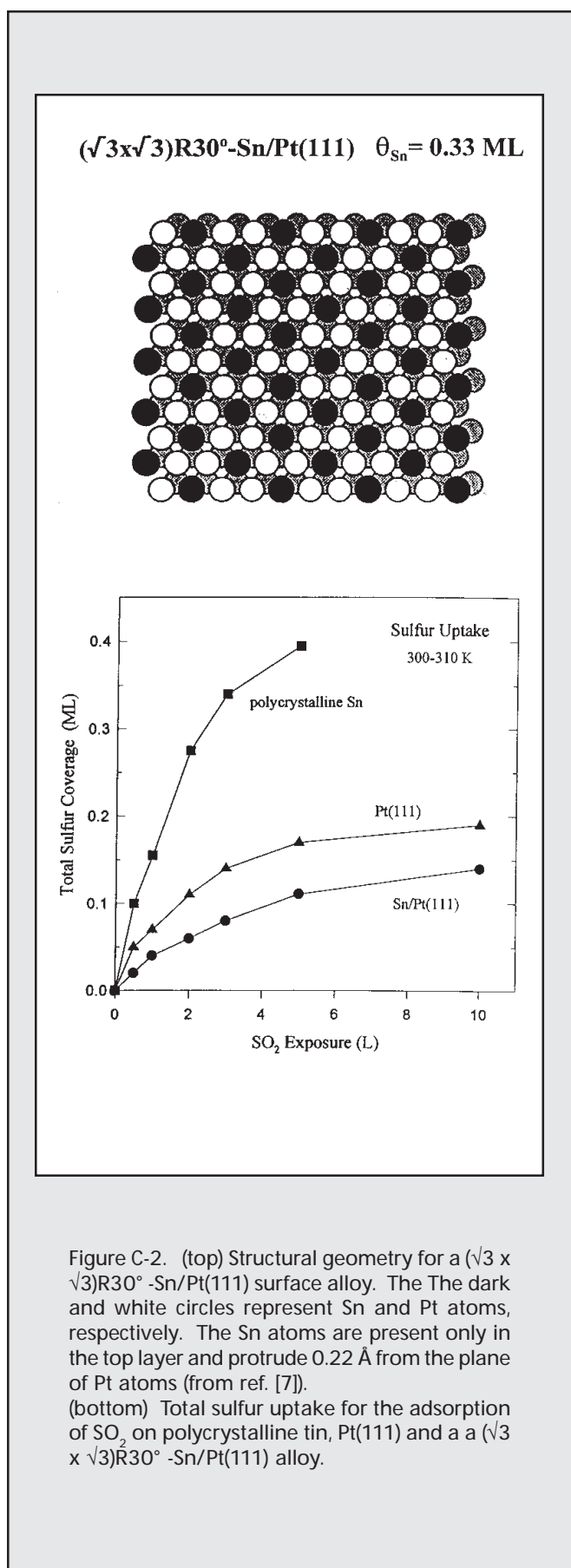


Figure C-2. (top) Structural geometry for a $(\sqrt{3} \times \sqrt{3})R30^\circ\text{-Sn/Pt(111)}$ surface alloy. The dark and white circles represent Sn and Pt atoms, respectively. The Sn atoms are present only in the top layer and protrude 0.22 Å from the plane of Pt atoms (from ref. [7]). (bottom) Total sulfur uptake for the adsorption of SO₂ on polycrystalline tin, Pt(111) and a $(\sqrt{3} \times \sqrt{3})R30^\circ\text{-Sn/Pt(111)}$ alloy.

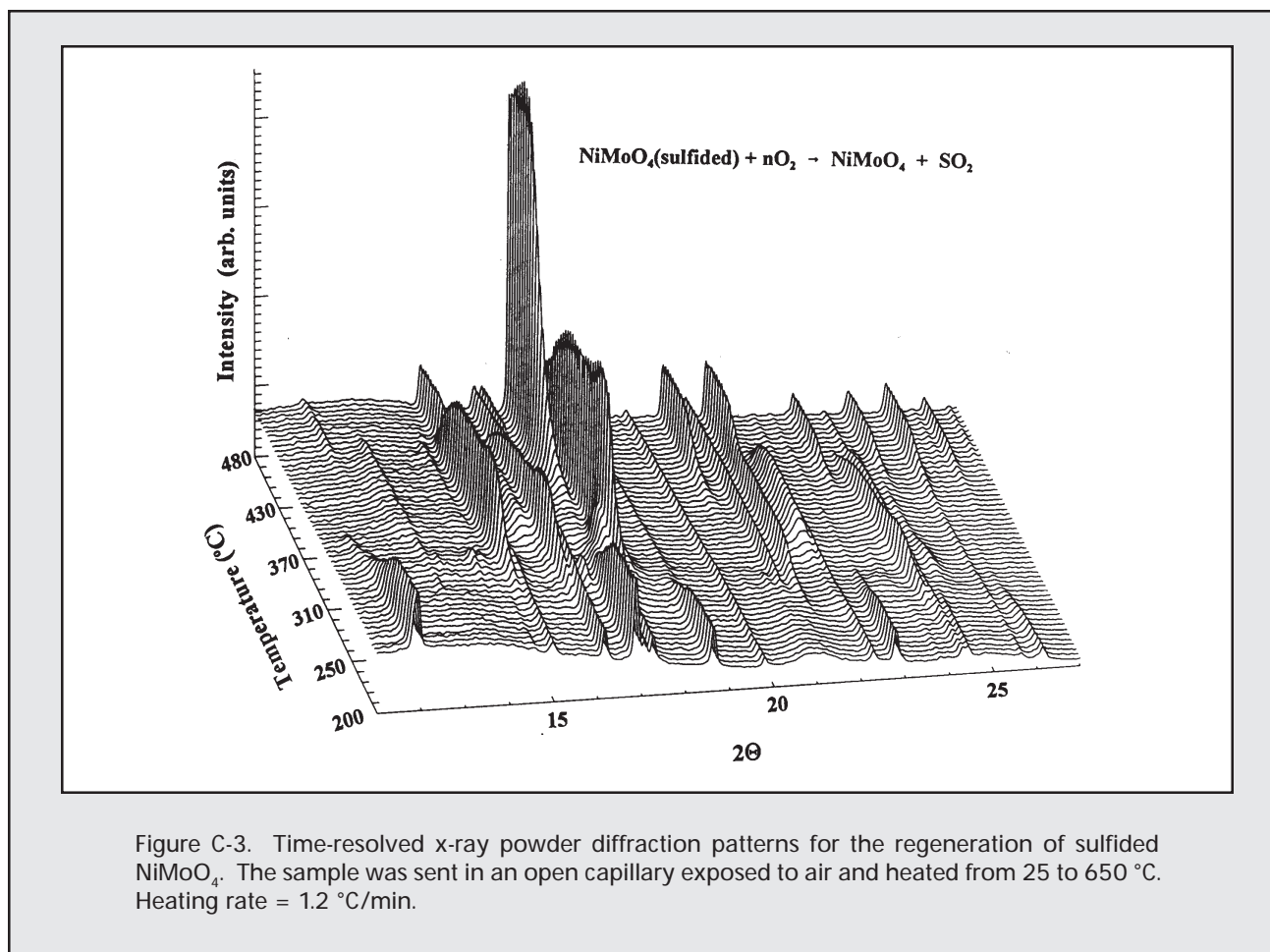


Figure C-3. Time-resolved x-ray powder diffraction patterns for the regeneration of sulfided NiMoO_4 . The sample was sent in an open capillary exposed to air and heated from 25 to 650 °C. Heating rate = 1.2 °C/min.

time-resolved XRD experiments under a wide variety of temperatures and pressure conditions ($-190\text{ °C} < T < 900\text{ °C}$; $P \leq 45\text{ atm}$).^[10] This unique approach has been used to study the regeneration of poisoned oxide catalysts.^[8,9] A typical case is shown in **Figure C-3**. After exposing a nickel molybdate (NiMoO_4) to H_2S , one sees the formation of metal sulfides and sulfates that change the x-ray diffraction pattern of the system.^[8,9] In the presence of O_2 this “mixture” is stable up to 250 °C when reaction begins.^[9] As the temperature is raised several

intermediates are observed, and at $\sim 400\text{ °C}$ the diffraction lines for pure NiMoO_4 appear. At 480 °C only the XRD pattern of NiMoO_4 is seen.^[8] Results of time-resolved XRD and XANES indicate that reaction with oxygen at high temperature is very effective for removing sulfur from poisoned NiMoO_4 , ZnO , NiO and MoO_3 catalysts. ■

This research was supported by the US Department of Energy, Division of Chemical Sciences, Office of Basic Energy Sciences.

REFERENCES

- [1] J.A. Rodriguez, T. Jirsak, S. Chaturvedi and J. Hrbek, *J. Am. Chem. Soc.*, **120**, 11149, (1998).
- [2] J.A. Rodriguez, T. Jirsak and S. Chaturvedi, *J. Chem. Phys.*, **110**, in press, (1999).
- [3] T. Jirsak, J.A. Rodriguez, S. Chaturvedi, and J. Hrbek, *Surf. Sci.*, **418**, 8, (1998).
- [4] T. Jirsak, J.A. Rodriguez and J. Hrbek, *Surf. Sci.*, submitted.
- [5] J.A. Rodriguez, S. Chaturvedi, T. Jirsak, and J. Hrbek, *J. Chem. Phys.*, **109**, 4052, (1998).
- [6] M. Kuhn, J.A. Rodriguez and J. Hrbek, *Surf. Sci.*, **365**, 53, (1996).
- [7] S.H. Overbury, D.R. Mullins, M.T. Paffett and B.E. Koel, *Surf. Sci.*, **254**, 45, (1991).
- [8] S. Chaturvedi, J.A. Rodriguez and J.L. Brito, *Catal. Lett.*, **51**, 85, (1998).
- [9] J.A. Rodriguez, S. Chaturvedi, J.C. Hanson, and J.L. Brito, *J. Phys. Chem. B*, in press.
- [10] P. Norby and J.C. Hanson, *Catal. Today*, **39**, 301, (1998).

Using X-Ray "Vision" to Understand Self-Assembly

P. Fenter (ANL), F. Schreiber (MPI-Stuttgart), A. Eberhardt (LANL),
 T.Y.B. Leung (U. Illinois, Urbana-Champaign),
 L. Berman (BNL-NSLS), M. Bedzyk (Northwestern U. and ANL),
 G. Scoles (Princeton U.), and P. Eisenberger (Columbia U.)

INTRODUCTION

The concept of "self-assembly" (SA) is derived from biological systems and can be defined as a process by which molecules having many internal degrees of freedom are able to form ordered supermolecular structures utilizing weak interactions such as van der Waals forces or hydrogen bonding^[1]. Monolayers of alkyl-thiols grown on Au(111) surfaces are special among the many self-assembling systems because this system is widely considered as prototypical and has many potential technical

applications. In this system the gold-sulfur bond is strong enough to anchor the molecules to the surface, yet at the same time this interaction leaves sufficient lateral mobility to allow the inter-chain van der Waals interaction to drive the system toward the formation of a stable well-ordered monolayer. Here we review some of the phenomena that we have uncovered using x-ray scattering techniques to study the growth of decanethiol (C10) on Au(111) surfaces from the vapor phase (for details of sample preparation, etc., see references^[2, 3, 4]).

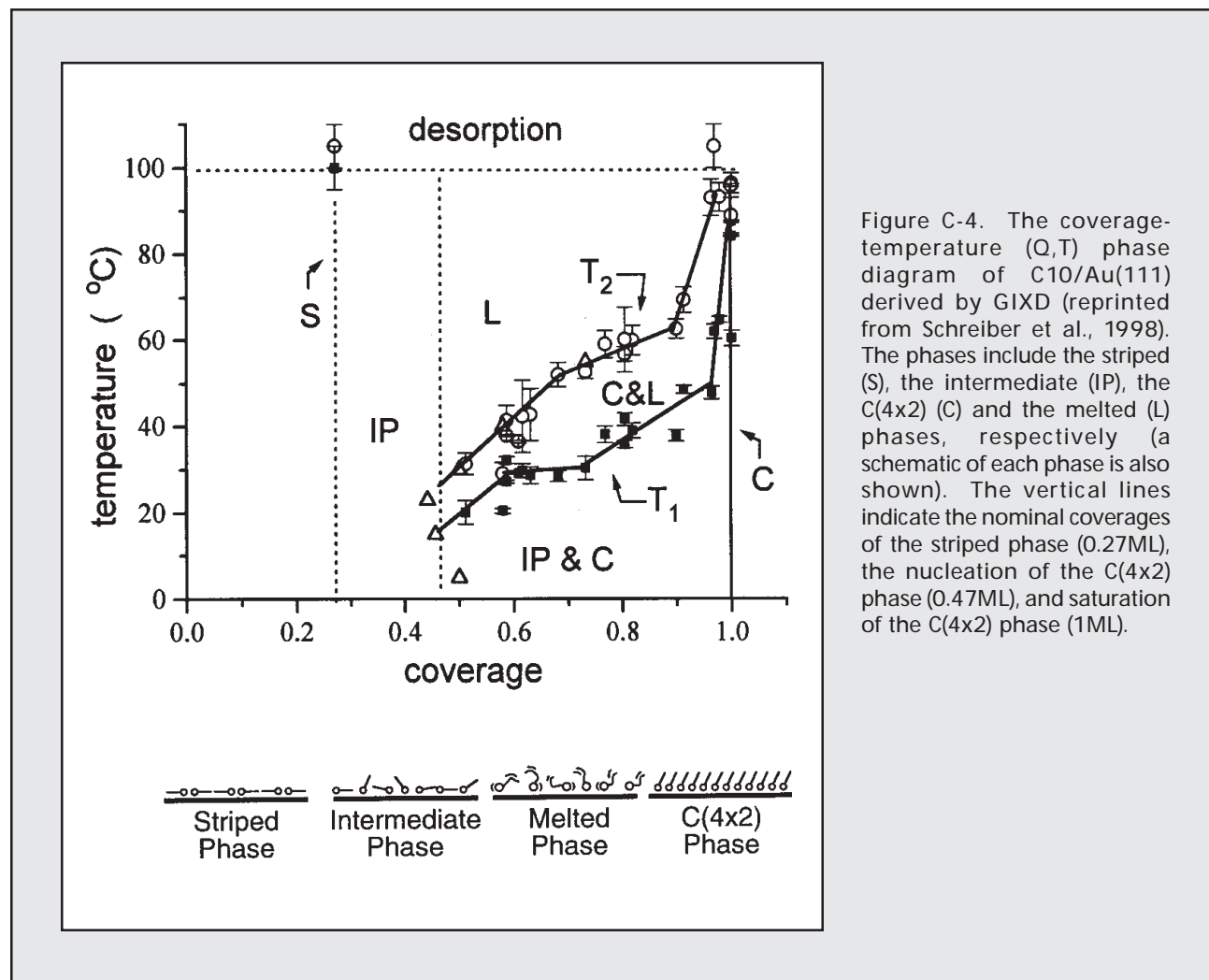


Figure C-4. The coverage-temperature (Q,T) phase diagram of C10/Au(111) derived by GIXD (reprinted from Schreiber et al., 1998). The phases include the striped (S), the intermediate (IP), the C(4x2) (C) and the melted (L) phases, respectively (a schematic of each phase is also shown). The vertical lines indicate the nominal coverages of the striped phase (0.27ML), the nucleation of the C(4x2) phase (0.47ML), and saturation of the C(4x2) phase (1ML).

PHASE BEHAVIOR OF SAMS

The first complexity that must be overcome is to understand the different equilibrium structures that are present during growth. Early growth studies have interpreted SAM growth as a continuous process by which the alkyl chains within the monolayer collectively transform from a disordered to an ordered configuration^[5]. Instead, through a combination of X-ray, He atom diffraction and scanning tunneling microscopy, it has been shown that there are a number of distinct phases present during the growth process^[3, 6]. In addition to the densely packed “standing up” C(4x2) phase at saturation coverage ($\Theta = 1 \text{ ML} = 4.6 \times 10^{14} \text{ molecules/cm}^2$), at low coverages a lying down “striped” phase ($\Theta = 0.27 \text{ ML}$) has been observed. By mapping out the temperature and coverage dependence of these two ordered phases using grazing incidence x-ray diffraction (GIXD), we have delineated^[3] the equilibrium phase behavior of this system (shown in **Figure C-4**). In addition to these two ordered phases there are at least two other *disordered* phases. There is an “intermediate” phase which is found at coverages intermediate between the C(4x2) and the striped phases (for $T < 15^\circ\text{C}$, with a nominal coverage of $\Theta = 0.47 \text{ ML}$), and a melted phase which apparently exists at all coverages for sufficiently elevated temperatures. Thus, at

equilibrium, the growth proceeds primarily through the *coexistence* of these distinct phases^[3].

A remarkable feature is that while a complete monolayer melts at $\sim 90^\circ\text{C}$, at $\Theta \sim 0.5 \text{ ML}$ the SAM melts at $\sim 15^\circ\text{C}$ (even though both phases are chemisorbed!). This dependence of T_m with Θ is one of the essential keys to understanding the SAM's ability to assemble into highly ordered structures^[3]. When growing in the presence of the melted phase ($T > 15^\circ\text{C}$) the order in the SAM (as measured by the average domain size) is substrate limited which is suggestive of significant diffusivity and Ostwald ripening of the growing islands. At lower temperatures ($< 15^\circ\text{C}$) the final SAM is significantly less ordered and the domain size evolution during growth is consistent with a fixed number of islands suggesting a loss of diffusivity at these temperatures^[3].

THE HEADGROUP-SUBSTRATE INTERFACE STRUCTURE AT THE BURIED INTERFACE

How can we understand the combination of high thermal stability coupled with an ability to assemble at, and even *below*, room temperature? This issue is closely related to the nature of the S-Au bond. While the vast majority of studies on these systems assume that the sulfur

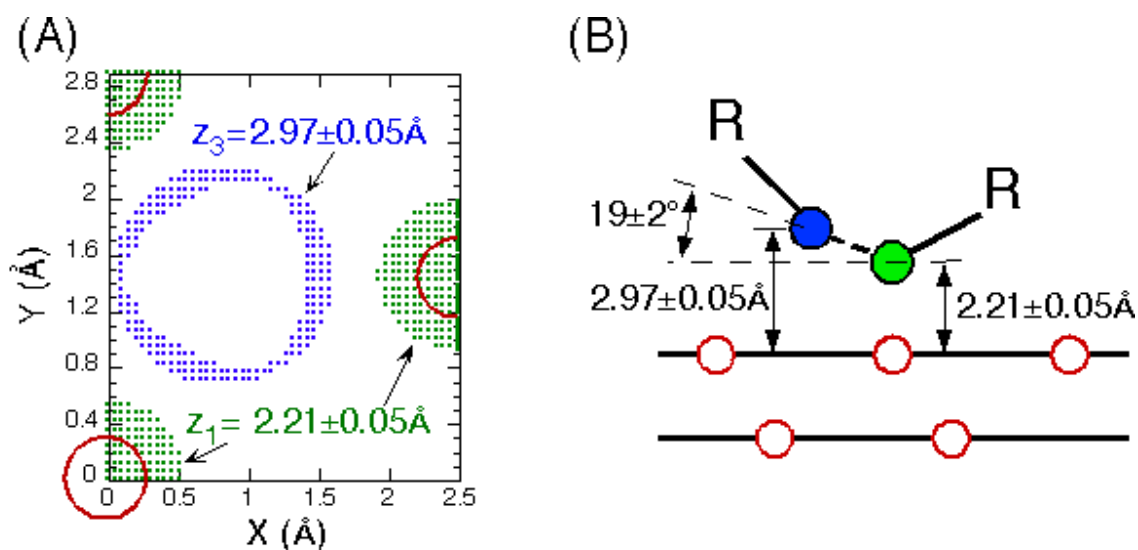


Figure C-5. (A) A map of the two sulfur head-group positions at heights of $z_1 = 2.21 \pm 0.05 \text{ \AA}$ (green), and $z_3 = 2.97 \pm 0.05 \text{ \AA}$ (blue) with respect to the underlying substrate lattice as derived from the XSW data for $\Theta = 1.0 \text{ ML}$. The large circles denote the Au substrate lattice sites. (B) A schematic of the derived “sulfur-dimer” structure, in which only one of the two head-groups interacts directly with the substrate (green circle). The hydrocarbon chains are schematically shown as “R” (adapted from Fenter et al., 1998).

headgroup bonds to the Au surface in an hexagonal $\sqrt{3} \times \sqrt{3} R30^\circ$ mesh with a S-S spacing of 5 Å^[7], our 2D crystallography results found that while the chain-chain spacing was indeed ~ 5 Å, the sulfur headgroups were instead arranged as sulfur dimers with a S-S spacing of ~ 2.2 Å^[8].

To resolve the ensuing controversy, we performed X-ray standing wave (XSW) measurements to directly probe the S/Au interface structure for this system^[2]. XSW is one of the few techniques which can directly and quantitatively probe a buried interface structure containing a low Z element such as sulfur by probing its XSW induced photoelectron yield near a substrate Bragg condition. The results (summarized in **Figure C-5**) reveal a highly detailed picture of the S-Au interface structure and directly contradict the widely assumed hexagonal S

mesh. We find that the two distinct S headgroup locations within the unit mesh each have a distinct height and lateral position^[2]. By combining these results with the information derived with GIXD^[8], we find that the S dimer is bound to the Au substrate through only one of the two S atoms with the presumed S-S bond being inclined by $19^\circ \pm 2^\circ$ with respect surface plane. The derived Au-S-S angle is consistent with the tetrahedral angle and therefore provides a natural context in which to understand the S-Au interface structure. The existence of a sulfur *dimer* species (which presumably interacts more weakly with a gold surface than a sulfur monomer) provides a simple yet plausible explanation for the observation of both a melted phase and significant surface diffusivity for these chemisorbed species at temperatures as low as 15°C.

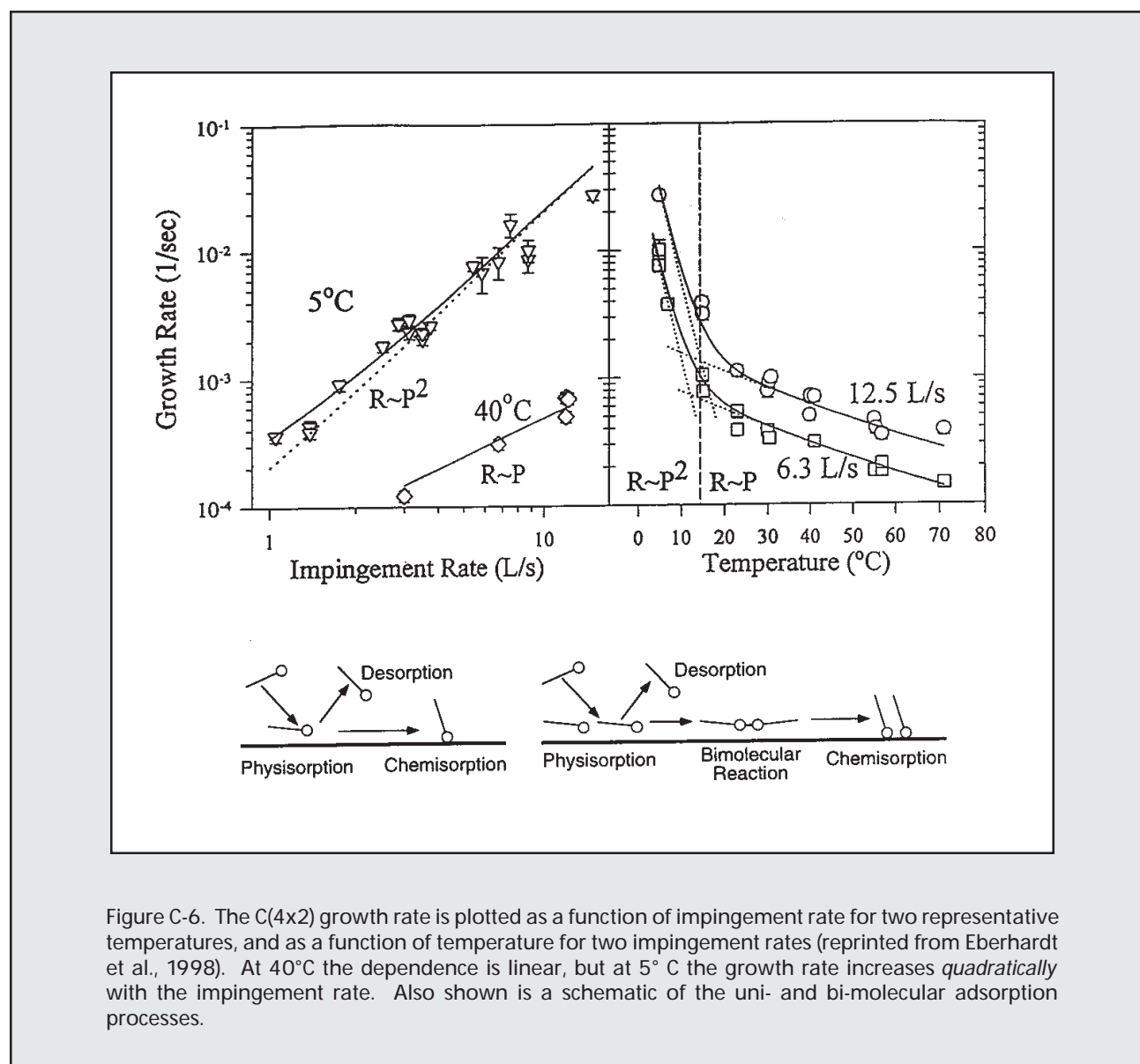


Figure C-6. The C(4x2) growth rate is plotted as a function of impingement rate for two representative temperatures, and as a function of temperature for two impingement rates (reprinted from Eberhardt et al., 1998). At 40°C the dependence is linear, but at 5°C the growth rate increases *quadratically* with the impingement rate. Also shown is a schematic of the uni- and bi-molecular adsorption processes.

ADSORPTION MECHANISMS IN SELF-ASSEMBLY

In this system, SA proceeds in a two-step fashion^[2,3], of which the second step is associated with the formation of the C(4x2) phase and the final “assembly” of the monolayer. We have made use of the simple proportionality between the GIXD integrated intensity and the coverage of a particular phase (the C(4x2) phase) to follow the growth kinetics *in situ* and in real-time, as a function of the thiol impingement rate and the substrate temperature^[4]. The data (**Figure C-6**) clearly show that there are two distinct adsorption processes, each having a distinct dependence upon temperature and pressure. From the decrease of the growth rate vs. increasing temperature in both processes, we can directly conclude that the molecules adsorb as a physisorbed precursor phase and thermalize before either chemisorbing or desorbing from the surface (i.e., physisorption mediated chemisorption)

A unique feature of these data is that while the high temperature process varies *linearly* with the impingement rate, the low temperature process varies *quadratically* with this quantity^[4]. While a linear variation is ubiquitous in surface adsorption and can be understood phenomenologically as the result of a uni-molecular process (i.e., each molecule adsorbs or desorbs independently of other molecules), the quadratic variation can be understood as an associative adsorption process, whereby the rate-limiting step is a *bimolecular reaction* in

the physisorption well:



where “p” and “c” denote physisorbed and chemisorbed species, respectively. This bimolecular adsorption process is very unusual and may ultimately be the result of the peculiar adsorption energetics of this system^[9].

CONCLUSIONS

X-ray scattering techniques have allowed us to unravel many of the molecular-level aspects of SA of C10 on Au(111). We conclude that the growth of this system can be understood in terms of its phase behavior, bonding, and adsorption mechanisms, and the complexity of this system is *not* a direct result of the molecular structure (e.g., as a result of chain entanglement), although chain entanglement is expected to be important for longer aliphatic molecules (e.g., polymer brushes). In work presently in progress^[9], we are testing our level of understanding of the SA process by probing the behavior of molecules that have two headgroups (e.g., hexanedithiol) and by investigating the influence of the molecular backbone rigidity. ■

The work described here was performed at the X10B and X24A beamlines. We thank Steve Bennett (X10B), Baoshan Zhang (X10B) and Barry Karlin (X24A) for their assistance during the measurements.

REFERENCES

- [1] G.M. Whitesides, J.P. Mathias and C.T. Seto, *Science*, **254**, 1312, (1991).
- [2] P. Fenter et al., *Surf. Sci.*, **412**, 213-235, (1998).
- [3] F. Schreiber et al., *Phys. Rev., B* **57**, 12476, (1998).
- [4] A. Eberhardt, P. Fenter and P. Eisenberger, *Surf. Sci. Letts.*, **397**, L285, (1998).
- [5] M. Grunze, *Physica Scripta*, **T49**, 711-717, (1993).
- [6] N.C. Camillone III et al., *J. Chem. Phys.*, **101**, 11031, (1994).
- [7] A. Ulman, *Chem. Rev.*, **96**, 1533, (1996).
- [8] P. Fenter, A. Eberhardt and P. Eisenberger, *Science*, **266**, 1216, (1994).
- [9] D.J. Lavrich, S.M. Wetterer, S.L. Bernasek and G. Scoles, *J. Phys. Chem., B* **102**, 3456-3465, (1998).
- [9] T.Y. Becky Leung, Ph.D. Thesis, Princeton University (1998); see the following web page for more information: www.princeton.edu/~gscoles.

Ionic States of Small Molecules Investigated by Vibrationally Resolved Core-level Photoelectron Spectroscopy

U. Hergenhahn, A. Rüdell, E.E. Rennie, K. Maier, B. Kempgens, H.M. Köppe,
and A.M. Bradshaw
(Fritz-Haber-Institute, Berlin, Germany)

Upon photoionization of a small molecule in the gas-phase, the excitation of one or several vibrational degrees of freedom is common. This occurs because the potential energy curve of the molecular ionic state is different from that of the neutral ground state. Since the photoionization process corresponds to a *sudden* change between the two states, the atomic core has no time to adiabatically respond to the change in conditions and is thus left in a state with potential energy. The ground state configurations of small molecules are usually well known and it is therefore possible to draw conclusions as to the nature of the excited state. This is especially true for the case of inner-shell ionization. However, the ability to record vibrationally resolved electron spectra at photon

energies sufficient to ionize an inner shell requires very good monochromatization of the incident light. In the last few years we have recorded core-level photoelectron spectra of several closed shell molecules at the X1B beamline^[1-3].

A good example of the determination of the ionic geometry in a closed-shell molecule is provided by the C 1s ionization spectrum of ethane (C_2H_6). Two vibrational progressions are visible in the C 1s photoelectron spectrum of C_2H_6 (**Figure C-7**). The first one, with vibrational energies around 400 meV, is typical for the photoionization of all small hydrocarbons and pertains to the totally symmetric C-H stretching vibrations. In terms of molecular geometries, excitation

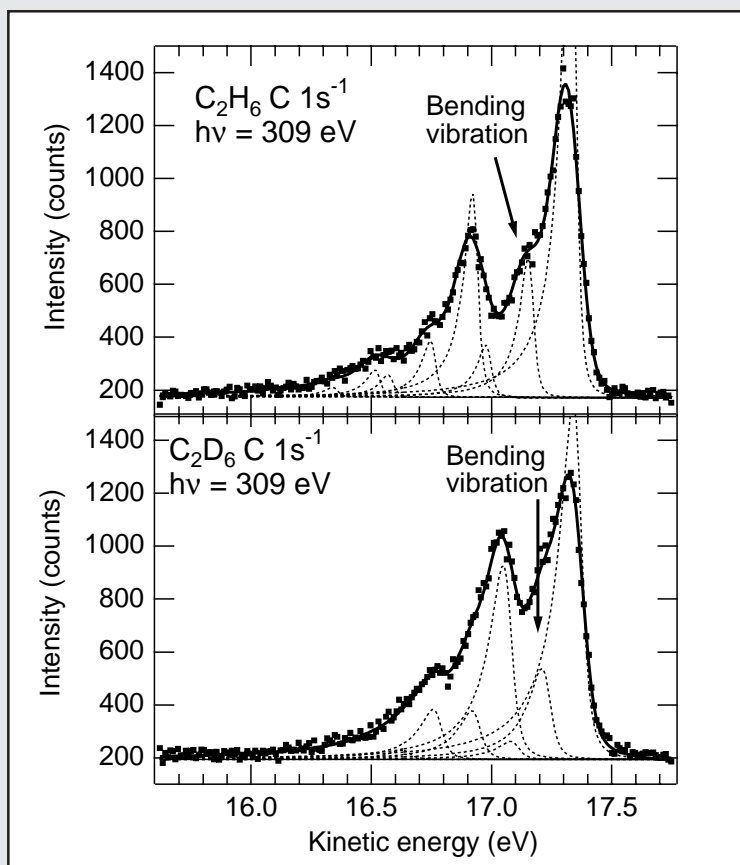


Figure C-7. C 1s photoelectron spectra of ethane and deuterated ethane measured with 309 eV photon energy at beamline X1B. The results of a least-squares fit assuming the excitation of only two normal vibrational modes have been included. The dashed lines represent the individual vibrational states, while the full line through the data points represents the fit result after summation and convolution with the instrument profiles.

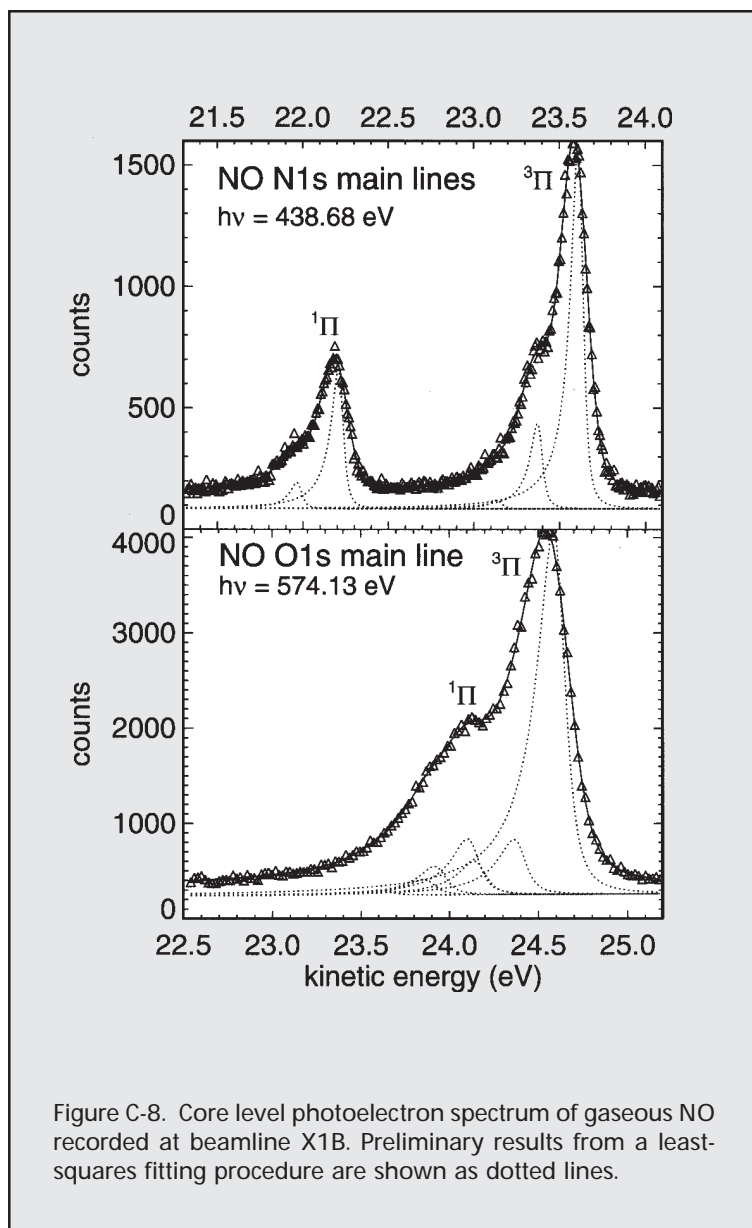


Figure C-8. Core level photoelectron spectrum of gaseous NO recorded at beamline X1B. Preliminary results from a least-squares fitting procedure are shown as dotted lines.

of this mode means that the C-H bond length shortens upon removal of the C 1s core electron. The second mode, with vibrational energies around 180 meV, was at first assigned to a totally symmetric C-C stretching vibration by several groups^[4]. However, calculations of the vibrational excitation probabilities have yielded the first evidence that another mode, namely an umbrella-like bending vibration of the hydrogens attached to the site of the core-hole, might play a stronger role than the movement of the two methyl groups against each other^[5]. By studying isotopically substituted ethane, C₂D₆, in parallel with C₂H₆, we have found that the frequency shift observed for the mode in question matches that of a C-H bending vibration, but not that of a CH₃-CH₃ stretching vibration. That is, the molecule changes its

C-C-H bond angle along with a change in C-H bond length. Quantitatively, vibrational energies of 176 ± 5 meV were found for this bending mode for ethane and 130 ± 10 meV for deuterated ethane. The C-H stretch was found to be 407 ± 5 meV and the C-D stretch to be 291 ± 10 meV. The changes in C-H bond length and C-C-H bond angle are 0.036 \AA and 2.1° , respectively, assuming a delocalized core hole^[6].

Molecular Species with an unpaired electron determine an important part of the chemistry of the atmosphere despite their generally low concentration. As a step towards the spectroscopic characterisation of these systems, we have recently measured inner-shell photoelectron spectra of the open-shell molecules O₂ and NO. Upon removal of an inner-shell electron, both of these molecules, will, in principle, show a photoelectron line split into two components by the exchange interaction between the unpaired electrons. The high-resolution photoelectron spectra of these systems can therefore give information on the influence of this spin-dependent force on the binding state of the molecular ions in play.

Turning to open shell molecules, we note that in the ground state configuration NO has an unpaired electron in the 2π orbital. Together with the spin 1/2 of an inner-shell hole, the molecular states $^1\Pi$ and $^3\Pi$ are thus formed. These states can be easily distinguished after ionization of an N 1s electron: our value for the exchange splitting is $1.40(1) \text{ eV}$ (**Figure C-8**). Both states show a similar vibrational progression, in which excitations

of up to two vibrational quanta can be seen. The vibrational energy from a preliminary analysis is around 240 meV for both spin states. This is similar to the value of 241 meV found for the N₂ N1s→ π^* excited neutral state^[3] and is much smaller than the value of 314(4) meV measured for inner-shell ionized N₂. A close similarity between NO and π^* -excited N₂ is expected from the Z+1 model. Less evident are the differences in exchange splitting, which can be seen by comparing the N 1s ionization spectrum with the O 1s spectrum. The triplet and singlet components of NO O1s⁻¹ overlap each other and the singlet peak can be seen as a shoulder about 0.48 eV away from the larger triplet peak. This splitting is, to our knowledge, resolved here for the first time and was earlier predicted to have a smaller value by theory:

The authors of [7] give values of 1.48 eV at the N-edge and 70 meV at the O-edge. A plausible explanation in chemical terms seems to be possible in this case: As oxygen has a higher electronegativity than nitrogen, the charge density of the bonding orbitals is stronger on the O side. Therefore, the anti-bonding lone π^* electron preferentially adheres to the N side and causes a stronger exchange interaction with a lone core electron at the same site. However relaxation, i.e. the reaction of the molecular charge cloud to the core hole creation, seems to substantially influence the charge distribution. Otherwise, the failure of theory to reproduce the splitting quantitatively would not be explainable.

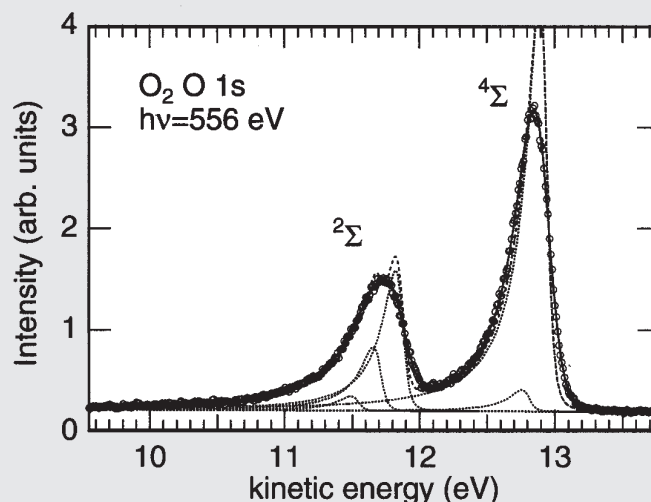
The inner-shell photoelectron spectrum of O_2 shows an easily observable separation into the $O\ 1s^{-1}\ ^2\Sigma$ and $^4\Sigma$ states (**Figure C-9**). An analysis of both lines reveals further differences. Although vibrational

components cannot be resolved for both of these lines, a significantly larger width of the $^2\Sigma$ component compared to the $^4\Sigma$ is clearly observed. A least squares fit results in a profile for the $^4\Sigma$ line which hardly shows any vibrational excitation. Interestingly, the $^2\Sigma$ line has vibrational components with a significantly larger spacing, 170(20) meV compared to 110(20) meV for the $^4\Sigma$ and larger excitation probability as well. One is therefore led to conclude that an ion with a stronger force constant and smaller bond-length is formed in the case of doublet ionized O_2^+ compared to quartet O_2^+ . This change in molecular potential is solely brought about by the different coupling between the lone inner-shell electron and the high-spin coupled $1\pi_g^2$ open valence shell. The high brightness of the X1B undulator has proved to be crucial in measuring high resolution core-level spectra of small molecules with high sensitivity. ■

REFERENCES

- [1] B. Kempgens, K. Maier, H. M. Köppe, M. N. Piancastelli, M. Neeb, and A. M. Bradshaw, *Phys. Rev. Lett.*, **79**, 998, (1997).
- [2] B. Kempgens, H. Köppel, A. Kivimäki, M. Neeb, L. S. Cederbaum, and A. M. Bradshaw, *Phys. Rev. Lett.*, **79**, 3617, (1997).
- [3] A. Kivimäki, K. Maier, U. Hergenhahn, M. N. Piancastelli, B. Kempgens, A. Rüdell, and A. M. Bradshaw, *Phys. Rev. Lett.*, **81**, 301, (1998).
- [4] H.M. Köppe *et al.*, *NSLS Annual Report*, (1996); S. J. Osborne *et al.*, *J. Chem. Phys.*, **106**, 1661, (1997).
- [5] T. D. Thomas, L. J. Saethre, S. L. Sorensen, and S. Svensson, *J. Chem. Phys.*, **109**, 1041, (1998).
- [6] E. E. Rennie, H. M. Köppe, B. Kempgens, U. Hergenhahn, A. Kivimäki, K. Maier, M. Neeb, A. Rüdell, and A. M. Bradshaw, *J. Phys. B*, **submitted**, (1998).
- [7] J. Müller and H. Ågren, in: *Proceedings of a NATO Advanced Study Institute on Molecular Ions*, edited by J. Berkowitz and K.-O. Groeneveld, Plenum Press, New York, Kos, Greece, **B90**, p. 221, (1980).

Figure C-9. $O\ 1s$ photoelectron spectrum of oxygen recorded at beamline X1B. Open dots are the data points, the solid line is the result of a least-squares fit for the total profile, while the dotted lines are results for the constituent components before convolution with the apparatus profile function.



X-ray Scattering from a Soluble Monolayer at the Water-Hexane Interface

M.L. Schlossman, Z. Zhang, D.M. Mitrinovic and S. M. Williams
(U. of Illinois, Physics and Chemistry Department)

Z. Huang
(NSLS)

Measurements of the microscopic structure of liquid interfaces or surfactant assemblies at these interfaces have utilized primarily one of two geometries: (1) macroscopic, single liquid-*vapor* interfaces at which the tail groups of surfactants are exposed to the vapor, and (2) multiple, microscopic liquid-liquid interfaces existing within surfactant solutions. A macroscopic single liquid-vapor interface is oriented by gravity and, in turn, orients surfactants supported on its surface. This allows for detailed structural measurements using, for example, either x-ray or neutron reflectivity or x-ray grazing incidence diffraction. However, surfactants at liquid-liquid interfaces in solution are in a chemical environment typically used for either man-made or biological applications. Recent efforts have combined the advantages of these two geometries in a third geometry, a macroscopic single liquid-liquid interface^[1-5]. In particular, our ability to flatten otherwise very curved interfaces allows x-ray surface scattering techniques to be used in the study of a wide range of liquid-liquid interfacial phenomena.

Here, we describe an x-ray surface scattering study of the structure of a monolayer of soluble surfactants at the water-hexane interface. The few available thermodynamic or spectroscopic measurements indicate that soluble and insoluble amphiphilic monolayers at water-oil interfaces are more loosely packed than the corresponding monolayers at the water-vapor interface^[6,7,8]. In particular, monolayers formed from surfactants soluble in the oil phase are expected to be disordered and in a liquid or gas phase at liquid-liquid interfaces^[8]. Contrary to this expectation, we find that soluble monolayers can form solid monolayer phases at the water-oil interface. In addition, the system described below exhibits a solid to gas phase monolayer transition at this interface. Comparison to a similar transition at the liquid-vapor interface indicates that the solvent acts to disorder the solid monolayer at the liquid-liquid interface at a lower temperature.

Monolayers of $F(CF_2)_{10}(CH_2)_2OH$ (denoted here as $FC_{12}OH$) self-assemble from a solution (2×10^{-3} mol/kg) in hexane onto the solution-water interface^[9, 10].

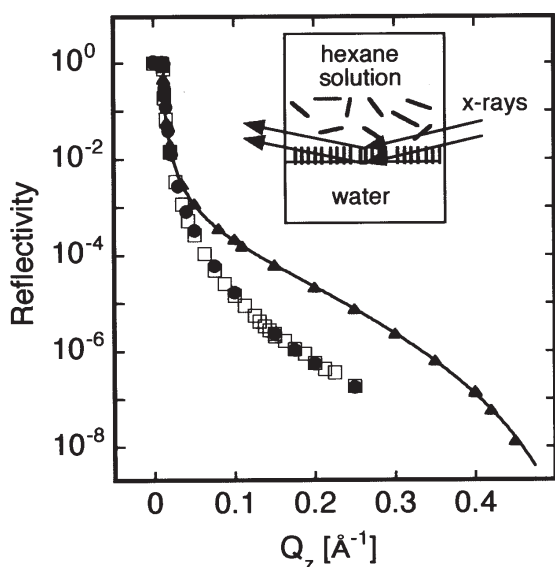


Figure C-10. X-ray reflectivity from the water-(hexane solution of $F(CF_2)_{10}(CH_2)_2OH$) interface at $T=32^\circ\text{C}$, triangles; $T=48^\circ\text{C}$, circles; pure water-hexane interface at $T=32^\circ\text{C}$, open squares. Inset is a cartoon of the solid surfactant monolayer that forms at $T=32^\circ\text{C}$. Also indicated are the x-rays reflecting off the top and bottom of the monolayer. The constructive interference of these x-rays is responsible for the increase in reflectivity.

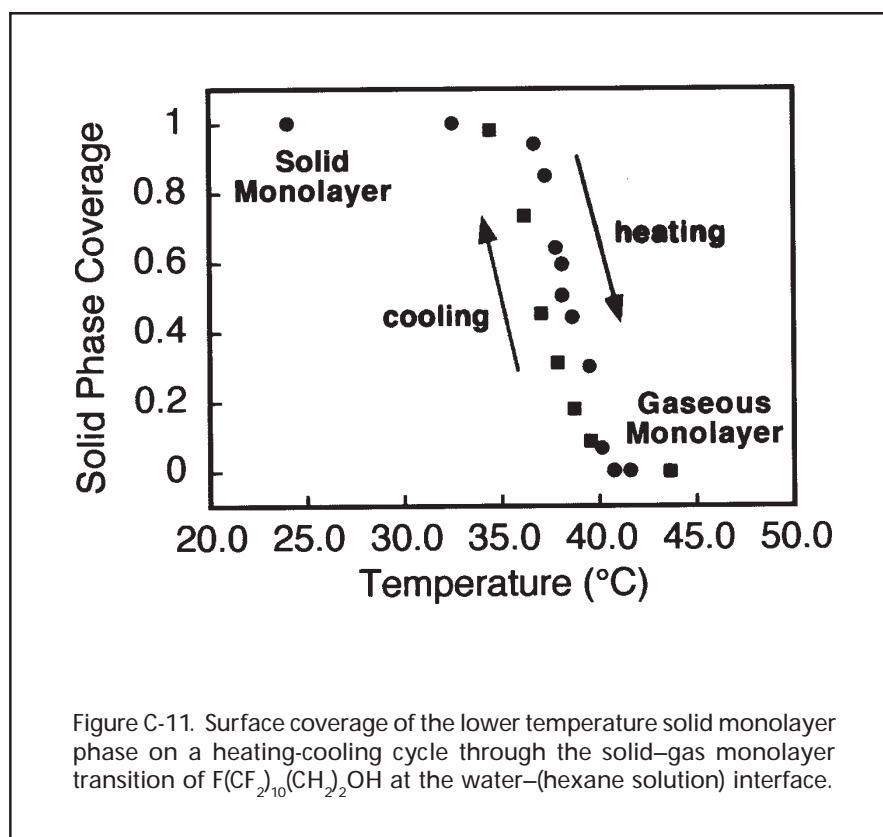


Figure C-10 illustrates x-ray reflectivity measurements at $T=32.00 (\pm 0.03)^\circ\text{C}$ from the monolayer at the water-(hexane solution) interface (plotted as a function of the wave vector transfer normal to the interface,

$Q_z = (4\pi/\lambda)\sin(\alpha)$, where $\lambda = 0.0825 \pm 0.0002$ nm is the x-ray wavelength for these measurements and α is the reflection angle measured from the plane of the interface). Also shown are measurements from the pure water-hexane interface at the same temperature and measurements from the water-(hexane solution) interface at $T=48.00^\circ\text{C}$. The enhanced reflectivity at higher Q_z from the water-(hexane solution) interface at $T=32.00^\circ\text{C}$ is due to a constructive interference of x-rays reflected from the top of the fluorinated monolayer with x-rays reflected from the bottom of the monolayer. The reflectivity from the water-(hexane solution) interface at $T=48.00^\circ\text{C}$ is nearly identical to the measurements from the pure water-hexane interface and indicates that most of the FC₁₂OH molecules have desorbed from the interface at this temperature^[11].

These data can be analyzed by using a general expression, derived from the first Born approximation for x-ray scattering, that relates the reflectivity to the electron density gradient normal to the interface, $\frac{d\langle\rho_e(z)\rangle}{dz}$ (averaged over the interfacial plane), and written as^[12]

$$\frac{R(Q_z)}{R_F(Q_z)} \cong \left| \frac{1}{\Delta\rho_{e,bulk}} \int dz \frac{d\langle\rho_e(z)\rangle}{dz} \exp(iQ_z z) \right|^2 \quad (1)$$

where $\Delta\rho_{e,bulk} = \rho_{e,bulk,lower} - \rho_{e,bulk,upper}$ and $R_F(Q_z)$ is the Fresnel reflectivity predicted for an ideal, smooth and flat interface^[13]. The layer of FC₁₂OH is modeled simply as a thin slab of higher electron density sandwiched between two bulk liquids. The interfaces of the top and bottom of this slab are roughened by thermal capillary waves, characterized by the roughness parameter, σ . The reflectivity calculated from Eq.(1) using the slab model for the electron density is fit to the data to yield values for the three fitting parameters: the slab thickness $L = 1.24 \pm 0.03$ nm, $\sigma = 0.36 \pm 0.02$ nm, and the fluorinated slab electron density (normalized to $\rho_{bulk\ water}$) $\rho_F = 1.90 \pm 0.04$ (**Figure C-10**)^[11].

Our measurement of the electron density of the monolayer at $T=32.00^\circ\text{C}$, $\rho_F = 1.90 \pm 0.04$, corresponds to a mass density of 2.19 ± 0.05 g/cm³. This agrees with the density of bulk solid fluoroalkane phases (e.g., for *n*-C₂₀F₄₂) which have a density of either 2.23 g/cm³ for the monoclinic crystal phase or 2.16 g/cm³ for the rhombohedral rotator solid phase^[14]. These measurements exclude the possibility that the FC₁₂OH monolayer at the water-hexane interface is in a liquid monolayer phase (bulk liquid fluoroalkanes have a mass density of approximately 1.7 g/cm³)^[14-16].

A similar analysis of the data from the water–(hexane solution) interface at $T=48.00^{\circ}\text{C}$ indicates that a conservative upper limit to the surface coverage of FC_{12}OH is approximately 1.5%^[11]. The transition from the solid FC_{12}OH monolayer to this gaseous monolayer at higher temperature can be studied by measuring reflectivity as a function of temperature. **Figure C-11** illustrates the first heating-cooling cycle through this transition. We believe that the transition region represents an interface with coexisting solid and gas monolayer phases. This is consistent with enhanced off-specular diffuse scattering that we measured in this transition region (not shown)^[17]. Accordingly, the reflectivity has been interpreted to yield the surface coverage of the lower temperature solid phase monolayer. Preliminary data indicate that the hysteresis in **Figure C-11** is reduced with further heating-cooling cycles through the transition temperature.

An important feature of studies of the liquid-liquid interface is the ability to characterize the role of the upper phase on the structural order within, for example, monolayers at the interface. To gain some insight into

the role of the upper-phase hexane on the ordering of the low temperature FC_{12}OH solid phase monolayers, we studied a similar transition in FC_{12}OH monolayers supported on the water-vapor interface. The FC_{12}OH monolayer was spread in the crystalline island phase at an inverse density of $0.4\text{ nm}^2/\text{molecule}$. Since the crystalline unit cell size is $0.29\text{ nm}^2/\text{molecule}$ there is excess area at the interface that allows the monolayer to undergo a transition to a liquid or gaseous disordered phase. X-ray grazing incidence diffraction measurements (not shown) indicate that a solid to gas (or, possibly liquid) monolayer phase transition occurs between 58.8°C and 62.09°C , slightly more than 20°C higher than the solid-gas transition in the FC_{12}OH monolayer at the water–(hexane solution) interface^[11]. Therefore, the presence of the hexane solvent acts to disorder the solid monolayer at a lower temperature. ■

This work was supported by the donors of The Petroleum Research Fund administered by the ACS, the UIC Campus Research Board, and the NSF Division of Materials Research.

REFERENCES

- [1] L.T. Lee, D. Langevin, and B. Farnoux, *Phys. Rev. Lett.* **67**, 2678, (1991).
- [2] J.S. Phipps, R.M. Richardson, T. Cosgrove, and A. Eaglesham, *Langmuir*, **9**, 3530, (1993).
- [3] B.R. McClain, *et al.*, *Phys. Rev. Lett.* **72**, 246, (1994).
- [4] M.L. Schlossman, *et al.*, *Rev. Sci. Instrum.* **68**, 4372, (1997).
- [5] S.M. Williams, Z. Zhang, D. Mitrinovic, Z. Huang, and M.L. Schlossman, in preparation, (1998).
- [6] B.Y. Yue, C.M. Jackson, J.A.G. Taylor, J. Mingins, and B.A. Pethica, *J. Chem. Soc. Faraday I* **72**, 2685, (1976).
- [7] M.C. Messmer, J.C. Conboy, and G.L. Richmond, *J. Am. Chem. Soc.*, **117**, 8039, (1995).
- [8] G.L. Richmond, *Analytical Chemistry* **69**, 536A, (1997).
- [9] Y. Hayami, A. Uemura, N. Ikeda, M. Aratono, and K. Motomura, *J. Coll. Int. Sci.* **172**, 142, (1995).
- [10] T. Takiue, *et al.*, *J. Phys. Chem.* **100**, 20122, (1996).
- [11] Z. Zhang, D.M. Mitrinovic, S.M. Williams, Z. Huang, and M.L. Schlossman, *J. Chem. Phys.*, in press (1999).
- [12] P.S. Pershan, *Far. Disc. Chem. Soc.* **89**, 231, (1990).
- [13] M. Born, and E. Wolf, *Principles of Optics*, (Pergamon Press, Oxford, 1980).
- [14] H. Schwickert, G. Strobl, and M. Kimmig, *J. Chem. Phys.* **95**, 2800, (1991).
- [15] PCR catalog (Gainesville, FL).
- [16] H.W. Starkweather, *Macromolecules* **19**, 1131, (1986).
- [17] D.M. Mitrinovic, M. Li, Z. Huang, and M.L. Schlossman, work in progress, (1999).